inorganics

MDPI

Article

Highly Transparent Yb:Y_2O_3 Laser Ceramics with High Thermal Conductivity Obtained via a Sintering-Additive-Free Strategy

Zhongchao Fu [1,2,*], Qiang Wu [1], Nan Wu [1,2], Haibo Long [1], Jinsheng Li [2], Yi Ren [2,3] and Zhaoxia Hou [1]

[1] Liaoning Province Key Laboratory of Micro-Nano Materials Research and Development, School of Mechanical Engineering, Shenyang University, Shenyang 110044, China; w52241163322@163.com (Q.W.); wunan20102010@163.com (N.W.); flydragon0109@163.com (H.L.); luckyxia2007@126.com (Z.H.)
[2] Key Laboratory for Anisotropy and Texture of Materials (Ministry of Education), Northeastern University, Shenyang 110819, China; lijinsheng@neuq.edu.cn (J.L.); ren.yi@cxtc.com (Y.R.)
[3] Fujian Changting Golden Dragon Rare-Earth Co., Ltd., Longyan 366300, China
* Correspondence: zhongchaofu@syu.edu.cn

Abstract

Fine-grained Yb:Y_2O_3 laser ceramics with excellent transmittance and thermal conductivity were fabricated from commercial powders. The process involved aqueous colloidal forming, additive-free air pre-sintering at 1400 °C, and hot isostatic pressing at 1550 °C. Suspensions were prepared with a deionization process to alleviate the hydrolysis issue, which optimizes the microstructure uniformity and enhances the green compacts' density after consolidation. The microstructure, in-line transmittance, microhardness, and fracture toughness of the Yb^{3+}-doped Y_2O_3 ceramics with different concentrations were measured. The 5.0 at% Yb^{3+}-doped Y_2O_3 ceramic yielded a superior transmittance of 80.1% at 1100 nm and 83.0% in the mid-infrared region. The average grain size was 752 nm. The sample exhibited a thermal conductivity of 9.94 $W \cdot m^{-1} \cdot K^{-1}$ while achieving a 1076 nm laser output with a 42 mW peak power and 4.3% slope efficiency.

Keywords: Yb:Y_2O_3; transparent ceramics; thermal property; optical property; colloidal processing

check for updates

Academic Editor: Kenneth J.D. MacKenzie

Received: 8 May 2025
Revised: 21 June 2025
Accepted: 25 June 2025
Published: 27 June 2025

Citation: Fu, Z.; Wu, Q.; Wu, N.; Long, H.; Li, J.; Ren, Y.; Hou, Z. Highly Transparent Yb:Y_2O_3 Laser Ceramics with High Thermal Conductivity Obtained via a Sintering-Additive-Free Strategy. *Inorganics* **2025**, *13*, 217. https://doi.org/10.3390/inorganics13070217

Copyright: © 2025 by the authors. Licensee MDPI, Basel, Switzerland. This article is an open access article distributed under the terms and conditions of the Creative Commons Attribution (CC BY) license (https://creativecommons.org/licenses/by/4.0/).

1. Introduction

Rare-earth-doped sesquioxide (Y_2O_3, Lu_2O_3, Sc_2O_3) transparent ceramics have attracted much attention thanks to their desirable properties such as the combination of physical and spectroscopic properties comparable to or surpassing the rare-earth-doped yttrium aluminum garnet (YAG), which is the most commonly used high-power solid-state laser material [1,2]. Among these, Y_2O_3 has been extensively studied over the past 40 years as a promising laser host material owing to its advantageous properties, including low cost, high corrosion resistance, low phonon energy, and superior absorption efficiency compared to Lu_2O_3 and Sc_2O_3 [3]. As for the active rare-earth ions, Yb^{3+} has simple two-energy manifolds, with wide absorption and emission bands, and possesses high quantum efficiency [4–6], operating in a quasi-three-level scheme, leading to few defects and much less heat generation and hence mitigating thermal loads while suppressing detrimental effects like up-conversion and excited-state absorption [7–12].

Over recent decades, there have been many green compacts' consolidating methods developed, among which the most commonly used is still dry pressing. Thus, starting from nanopowders obtained by wet-chemical methods after calcination, green compacts were consolidated through dry pressing [13–16]. Nevertheless, colloidal processing is

widely recognized to offer significant advantages over dry pressing, including improved sinterability and providing versatile geometrical options to broaden the scope of application [17–19]. However, Y_2O_3 particles exhibit high reactivity in aqueous media, and the dissolved ions from the hydrolysis process pose difficulties in preparing well-dispersed, high-solid-loading suspensions [20–23]. Recently, we demonstrated that deionization during the suspension preparation offers an effective solution to suppress Y_2O_3 particle hydrolysis during suspension preparation. Green compacts consolidated from 35.0 vol% solid-load suspensions exhibited enhanced microstructure uniformity, high relative density, and improved sinterability.

It is well accepted that achieving ceramics with high optical properties is generally linked to a maximal elimination of residual pores. Meanwhile, a small-sized grain is also favorable to achieving enhanced thermal shock resistance and mechanical strength. A comprehensive review of the published literature reveals limited research on the fabrication of highly transparent Yb:Y_2O_3 ceramics by adopting nanopowders obtained by wet-chemical methods as a starting powder; green compacts were consolidated through traditional dry pressing; and transparent ceramics were prepared through a two-step densification process combining vacuum pre-sintering with subsequent hot isostatic pressing (HIP) and longtime annealing at a high temperature with ZrO_2 as the sintering additive. In many recent studies, various sintering additives [15,24,25] were adopted to promote densification and control the grain growth during the sintering process to achieve Yb^{3+}-doped Y_2O_3 transparent ceramics with improved optical and mechanical properties. Among them, ZrO_2 [8,26–30] has been proven as an effective additive and has been widely used. However, the introduction of sintering additives to the host matrix usually causes valence imbalance and disturbed lattice arrangement, leading to the reduction in phonon mean free path, ultimately degrading laser performance through significant thermal conductivity deterioration [31], laser-induced photodarkening [26,32], and the "orange peel" effect [33]. The thermal conductivity of gain media is one of the most important from both fundamental and applied perspectives for high power laser. According to Liu's research [34], the pure fine-grained Y_2O_3 ceramic exhibits a room-temperature thermal conductivity of 12.72 $W{\cdot}m^{-1}{\cdot}K^{-1}$; however, the 5.0 at% ZrO_2-doped samples sharply reduced to 7.02 $W{\cdot}m^{-1}{\cdot}K^{-1}$. However, despite a large amount of research, the fabrication of transparent laser ceramics without additives has been reported relatively little. The technique of vacuum sintering plus HIP is quite complicated, and the high cost of the equipment, especially for vacuum sintering and long-time high-temperature annealing, restricts the commercial production of the material. In our previous work [35] mentioned above, highly transparent Y_2O_3 ceramics were fabricated using low-temperature air pre-sintering followed by HIP; the transmittance of the sample reached 83.3% at 1100 nm; and an average grain size of 690 nm was achieved, which is convenient and easy. There is, however, to the best of our knowledge, no other published research of colloidal processing combining air pre-sintering and HIP for the fabrication of Yb^{3+}-doped Y_2O_3 ceramics. It is also worth mentioning that the doping of Yb^{3+} into a Y_2O_3 lattice would cause energy transfer to impurities, color centers, and lattice distortion, or concentration quenching to the upper state that nonradiatively decays even the additional non-linear heat generation in Yb:Y_2O_3 ceramics [36]. However, systematic research on Yb-doped Y_2O_3 ceramics regarding their optical, mechanical, and thermal properties has been little reported.

In this work, we synthesized Y_2O_3 nanopowders with various Yb^{3+} concentrations using the solid-state reaction from commercial powders, and fine-grained and highly transparent Yb^{3+}-doped Y_2O_3 ceramics with high thermal conductivity were achieved via aqueous colloidal processing and combined air pre-sintering with the HIP sintering method without a sintering additive. Stable suspensions were obtained via an optimized

deionization process before consolidation. The optical, thermal, mechanical, and laser properties and microstructures of the samples were systematically investigated in detail to enable the broader use of the high-energy and -efficiency Yb^{3+}-doped Y_2O_3 ceramics.

2. Results and Discussion

2.1. Powder Phase and Morphology

Integrated X-ray diffraction patterns of Yb^{3+}-doped Y_2O_3 powders with different concentrations after calcination at 1100 °C are shown in Figure 1. Each peak position of different concentrations of the Yb^{3+}-doped Y_2O_3 powder matches well with the cubic Ia3 space group structure of the Y_2O_3 crystal phase (ISCD No. 79-1716), implying the complete dissolution of Yb^{3+} ions into the Y_2O_3 host lattice without forming secondary phases. It is worth mentioning that the shift in the diffraction peaks was barely observed due to the similar ionic radii between Y^{3+} (r = 0.89 Å) and Yb^{3+} (r = 0.84 Å).

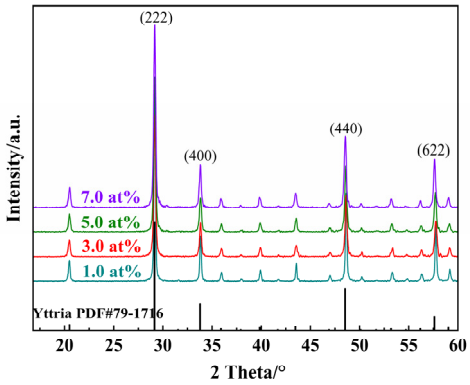

Figure 1. XRD spectrum of Yb^{3+}-doped Y_2O_3 powders with different concentrations after calcination.

Figure 2 presents the TEM photographs of the Yb^{3+}-doped Y_2O_3 powders after calcination at 1100 °C. All the powders doped with Yb^{3+} were composed of quasi-spherically shaped particles, indicating the isotropic structure of the particles. With the increase in Yb^{3+} concentration from 1.0 to 7.0 at%, the average particle size of the powder increased from 51 ± 2 nm to 65 ± 4, 64 ± 3, and 72 ± 3 nm, respectively, revealing that the doping of Yb^{3+} could accelerate the diffusion rate and promote the growth of particles during calcination. Further observation reveals that the powder exhibited slight agglomeration and few large-sized particles, which was caused by incomplete ball-milling dispersion, failing to achieve high dispersion, and different diffusion rates during the calcination process occurred.

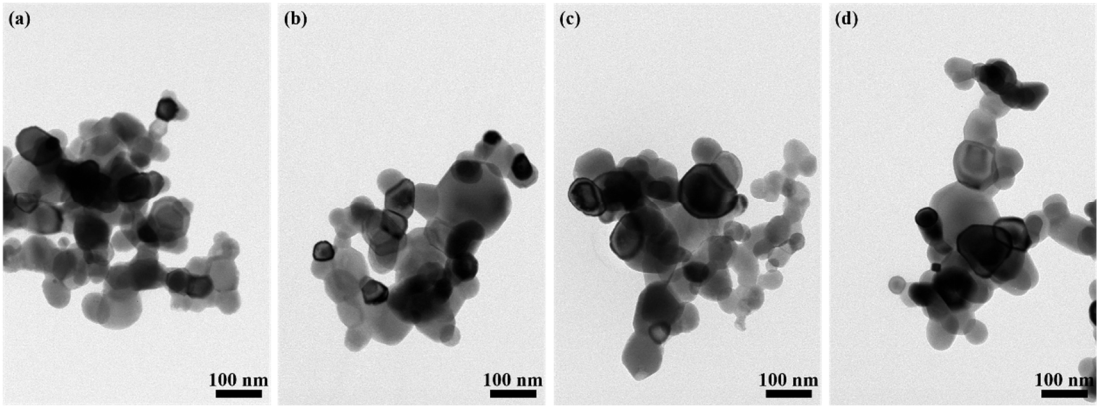

Figure 2. TEM images of Yb^{3+}-doped Y_2O_3 powder with different concentrations after calcination: (**a**) 1.0 at%, (**b**) 3.0 at%, (**c**) 5.0 at%, (**d**) 7.0 at%.

2.2. Dispersion Behavior of Yb^{3+}-Doped Y_2O_3 Powders

It is well known that the dispersity state of the particles in the suspension directly determines the homogeneity and packing density of the green compacts [37]. Figure 3 presents the particle size distributions for both suspension types (5.0 at% Yb^{3+} representative samples) at 10 wt% solid loading, comparing the deionization states before and after 2 h of stirring. The non-deionized suspension exhibits a broad size distribution (0.2–3.9 μm) with a mean particle diameter of 1.18 μm. In contrast, particles of the sample after deionization display a significantly smaller average particle size of 411 nm and narrower size distribution of 0.1–1.5 μm. The narrow particle size distribution is beneficial for achieving high-solid-loading and low-viscosity colloidal suspensions, thereby enhancing both the homogeneity and density of the consolidated green compacts. Meanwhile, the zeta-potential values of the suspensions at 10 wt% solid loading for the different concentrations of Yb^{3+} (1.0, 3.0, 5.0, 7.0 at%) at a pH of 10 with 1.25 wt% TAC added as dispersant are 53.4, 55.5, 54.8, and 56.4 mV, respectively. The elevated zeta potential suggests substantial surface charges and pronounced electrostatic repulsion between particles, which effectively stabilizes the colloidal system [38].

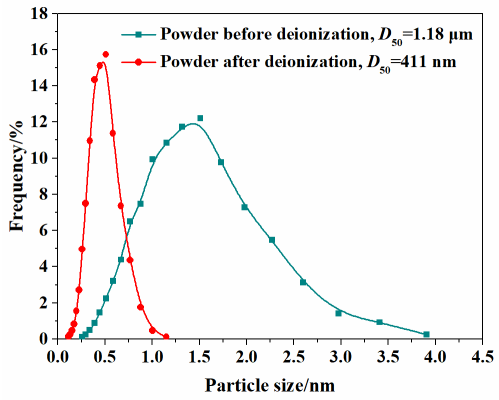

Figure 3. Particle size distributions of the 5.0 at% Yb^{3+}-doped Y_2O_3 suspensions before and after the deionization.

As is well known, the attainment of homogeneous green compacts with high relative density and minimal defects fundamentally requires suspensions exhibiting three key characteristics: optimized rheological behavior, high solid loading, and excellent colloidal stability. Figure 4 presents the rheological behavior of stabilized suspensions (35.0 vol% solid loading), demonstrating the relationship between apparent viscosity and shear rate after milling for 8 h with 1.25 wt% TAC added. Rheological analysis reveals quasi-Newtonian behavior, with viscosity decreasing linearly from 19.0 mPa·s (at 0.1 s^{-1}) to 9.0 mPa·s (at 100 s^{-1}), indicating a well-dispersed suspension. The relative densities of the green compacts with different Yb^{3+} concentrations (1.0, 3.0, 5.0, 7.0 at%) are 51.8%, 50.4%, 51.4%, and 51.3%, respectively, which is favorable for full densification at low temperatures during sintering.

As mentioned above, Y_2O_3 powders exhibit high reactivity in aqueous media, and the adsorption of dissolved cations onto negatively charged particle surfaces leads to electrical double layer compression, consequently diminishing interparticle electrostatic repulsion. Herein, the thickness of the electrical double layer is evaluated, based on the Gouy–Chapman model [39,40] of the electrical double layer with the Debye–Huckel approximate equation, and the potential at a random point in the diffuse layer ψ is given by

$$\psi = \psi_0 \exp(-\kappa x) \quad (1)$$

where ψ_0 is the surface potential of the particle; κ is the Debye–Huckel constant; $1/\kappa$ is the thickness of the electrical double layer, which is only related to the temperature and electrolyte concentration of the suspension; and x is the distance from the surface of the particle. The thickness of the electrical double layer of the aqueous solution of a covalent electrolyte at room temperature is given by

$$1/\kappa = \frac{1}{1.039 \times 10^8 \left(cZ^2\right)^{1/2}} \quad (2)$$

where c is the concentration of the ions and Z is the total number of valence electrons of the electrolyte. Taking the 5.0 at% Yb:Y_2O_3 suspension as an object, we approximated that it only produced ions of Y^{3+}, and the concentrations of dissolving ions of the untreated suspension and the deionized suspension after 2 h of milling were 1.76×10^{-5} mol/L and 5.14×10^{-6} mol/L, respectively. Additionally, the influence of surface properties including surface charge density and particle size was taken into account for the case of their particle radius being larger than the Debye–Huckel length. The thickness of the electrical double layer could be optimized as follows:

$$\delta_s \approx 3.68 1/\kappa \quad (3)$$

where δ_s is the optimized thickness of the electrical double layer [41]. Finally, the thickness of the electrical double layer of the deionized suspension was 18.0 nm, twice as thick as the untreated suspension (9.6 nm), and the repulsion of the potential energy was also raised to prevent the particles from coalescing. From the results we have obtained, one can conclude that the deionization process is an easy way for the preparation of a well-dispersed Y_2O_3 suspension with high solid loading.

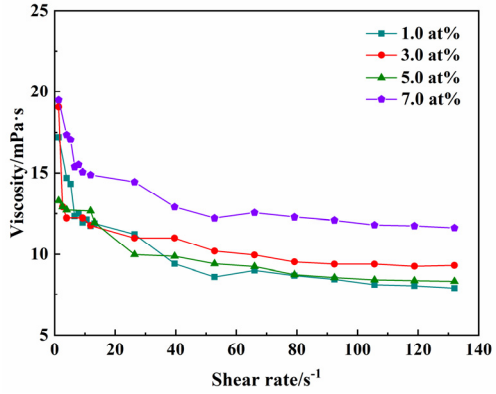

Figure 4. The viscosity of different concentrations of Yb^{3+}-doped Y_2O_3 suspensions at a solid loading of 35.0 vol% with 1.25 wt% TAC added.

2.3. Morphology, Optical, Mechanical, Thermal, and Laser Properties of Yb^{3+}-Doped Y_2O_3 Transparent Ceramics

Figure 5 shows SEM images of the 1.0, 3.0, 5.0, and 7.0 at% Yb^{3+}-doped Y_2O_3 air pre-sintered at 1400 °C for 16 h, and the relative densities of the samples were 96.7%, 96.9%, 97.0, and 97.2%, respectively. The average grain size of the samples was in the range of 400–500 nm. As we can see, there were no open pores observed, and the residual closed pores with a size < 300 nm were attached to the grain boundaries, which was in the final stage of sintering and very favorable for the following HIP process for densification. Figure 6 presents SEM micrographs of transparent ceramics after 1550 °C for 2 h under an Ar gas pressure of 200 MPa during HIP followed by thermal etching at 1500 °C for 1 h in the air. The narrow grain boundaries without any pores indicate that the sample

was fully densified. All the samples possessed a relatively small grain size, without the presence of abnormal grains. The EDS mapping in Figure 7 confirms the homogeneous elemental distribution (Y, O, Yb) throughout the 5.0 at% Yb:Y_2O_3 ceramic matrix, with no grain boundary segregation, a uniform triple junction composition, and successful Yb^{3+} incorporation into the host lattice. The apparent white dots in panel (c) represent instrumental artifacts from SEM detection limits.

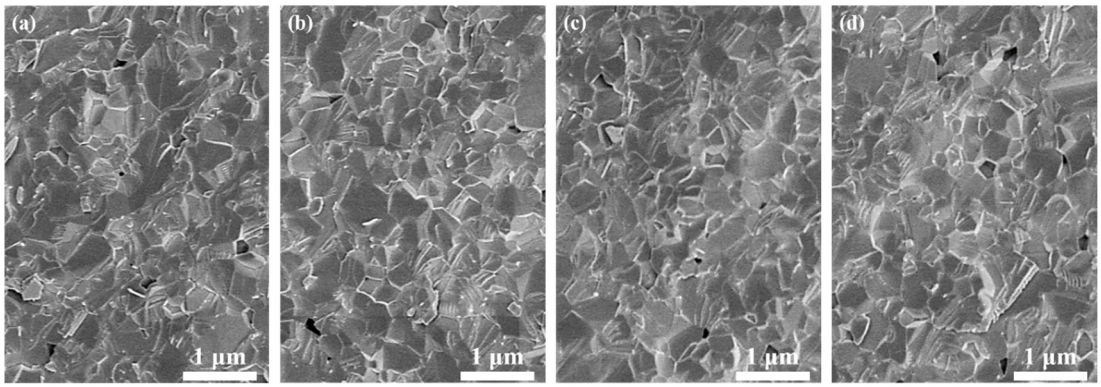

Figure 5. SEM images of the fracture surfaces of the Yb^{3+}-doped Y_2O_3 sintered compacts after air pre-sintering at 1400 °C for 16 h: (**a**) 1.0 at%, (**b**) 3.0 at%, (**c**) 5.0 at%, and (**d**) 7.0 at%.

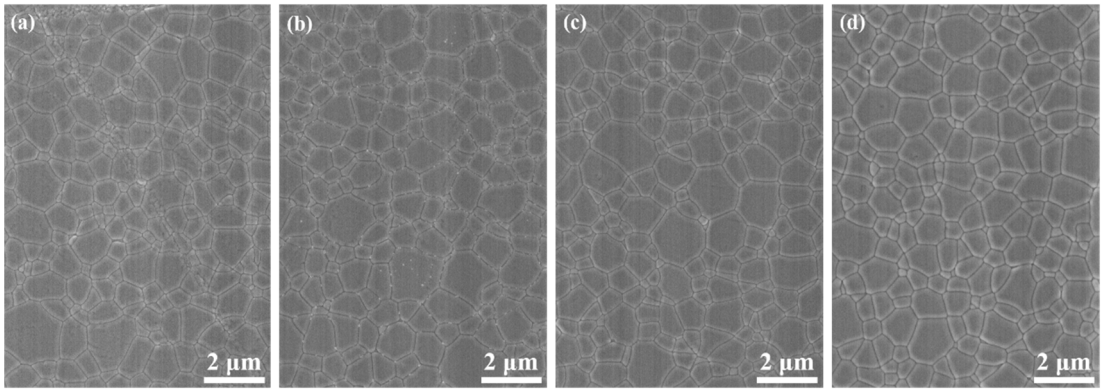

Figure 6. SEM images of Yb^{3+}-doped Y_2O_3 transparent ceramics after HIP and thermal etching: (**a**) 1.0 at%, (**b**) 3.0 at%, (**c**) 5.0 at%, and (**d**) 7.0 at%.

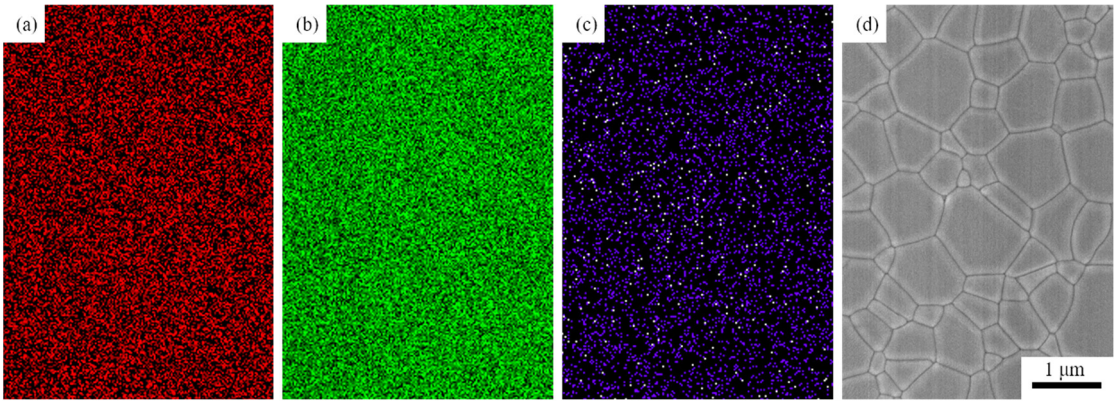

Figure 7. EDS mapping of O, Y, and Yb and SEM image of 5.0 at% Yb^{3+}-doped Y_2O_3 transparent ceramic: (**a**) EDS of O-Kα, (**b**) EDS of Y-Kα, (**c**) EDS of Yb-Kα, and (**d**) SEM image of ceramic.

Figure 8 displays a photograph of the polished Yb^{3+}-doped Y_2O_3 transparent ceramics obtained by air pre-sintering plus HIP treatment without annealing. It can be seen that all

specimens are fully transparent, and the words under the samples can be seen clearly. The in-line transmittance spectra are shown in Figure 9, and all the samples have an excellent optical transmission in both the near-infrared and the visible region. Figure 9a shows the in-line transmittance of the Yb^{3+}-doped Y_2O_3 transparent ceramics at wavelengths ranging from 200 to 2000 nm. The absorption multi-peaks appear centered around 980 nm, referring to the transition of Yb^{3+} from the ground state of $^2F_{7/2}$ to the excited state of $^2F_{5/2}$ [42]. The in-line transmittance of the samples increases with the increase in Yb^{3+} concentration to 5.0 at%, which reaches 80.1% at 1100 nm, and then slightly decreases when the Yb^{3+} content reaches 7.0 at%. The infrared transmittance curve of the samples within the 2.0–10.0 μm wavelength range is illustrated in Figure 9b. With the increase in the Yb^{3+} concentration from 1.0 to 5.0 at%, the transmittance in the near-infrared and mid-infrared region increases slightly. The Y_2O_3 sample doped with 5.0 at% Yb^{3+} achieves a mid-infrared transmittance as high as 83.0%. This combination of wide transmission range and high transparency positions the Yb:Y_2O_3 ceramic as an exceptional candidate for infrared optical applications.

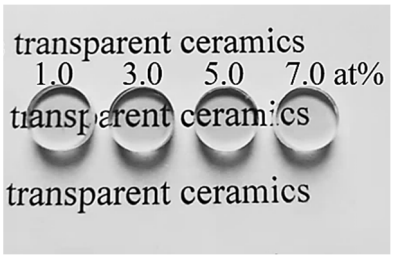

Figure 8. Photographs of the transparent ceramics after polishing.

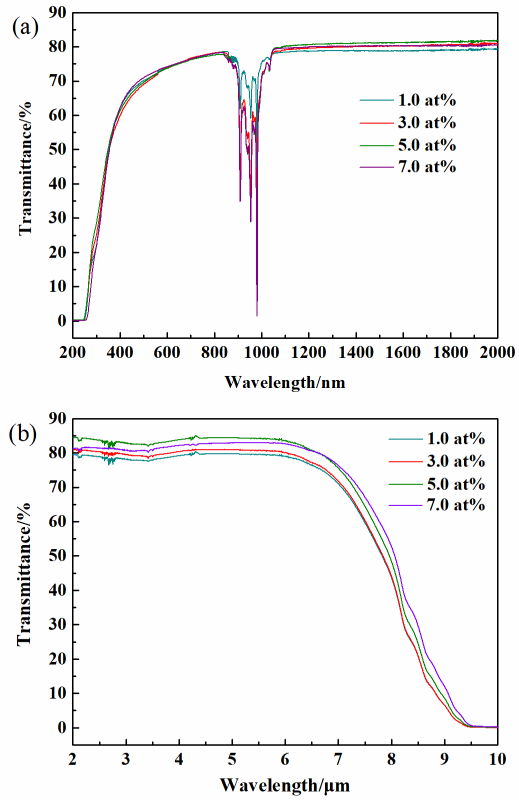

Figure 9. In-line transmittance of Yb^{3+}-doped Y_2O_3 ceramics with different concentrations after HIP: (**a**) in the range of 200–2000 nm and (**b**) in the range of 2.0–10.0 μm.

In addition to the optical properties, thermal and mechanical properties also serve as crucial evaluation criteria for transparent ceramics. Superior mechanical strength and

damage tolerance are essential for ensuring ceramic reliability and machinability. Table 1 displays the average grain size, Vickers hardness (*H*v), and fracture toughness (K_{IC}) of sintered Yb:Y_2O_3 transparent ceramics doped with various Yb^{3+} concentrations. The synthesized Yb:Y_2O_3 transparent ceramics consistently exhibited sub-micrometer grain sizes (from 700 nm to 760 nm), with a modest grain coarsening observed at higher Yb^{3+} concentrations (from 1.0 to 7.0 at%). Counterintuitively, microhardness values exhibited a slight decline from 8.2 GPa to 8.1 GPa with increasing doping levels, while fracture toughness showed a negligible concentration dependence.

Table 1. Average grain size, microhardness, and fracture toughness of Y_2O_3 transparent ceramics with different concentrations of Yb^{3+} doped.

Concentration of Yb^{3+} (at%)	Average Grain Size (nm)	Microhardness (GPa)	Fracture Toughness, K_{IC} ($MPa \cdot m^{1/2}$)
0.0 [35]	690 ± 20	8.36 ± 0.03	1.01 ± 0.02
1.0	701 ± 24	8.22 ± 0.06	1.00 ± 0.03
3.0	722 ± 22	8.20 ± 0.05	0.99 ± 0.05
5.0	752 ± 25	8.13 ± 0.07	0.98 ± 0.05
7.0	761 ± 19	8.10 ± 0.03	0.99 ± 0.05

Table 2 summarizes the thermal conductivity of the 5.0 at% Yb:Y_2O_3 transparent ceramic compared to the reported values in the open literature. With the decreased amount of sintering additives adopted for the sintered ceramics, the thermal conductivity increased from ~6.5 to 8.84 $W \cdot m^{-1} \cdot K^{-1}$. In agreement with theoretical predictions, the thermal conductivity measured for our sintering-additive-free 5.0 at% Yb:Y_2O_3 transparent ceramic was 9.94 $W \cdot m^{-1} \cdot K^{-1}$, which is the highest ever reported to the best of our knowledge, and the improved thermal shock resistance is the most beneficial to high-power laser output. It is worth mentioning that the thermal conductivity in this study is still lower than the theoretical value of Y_2O_3 transparent ceramics (13.6 $W \cdot m^{-1} \cdot K^{-1}$) [33,43], which is ascribed to energy transfer to impurities, color centers, and lattice distortion, or concentration quenching to the upper state that nonradiatively decays even the additional non-linear heat generation in Yb:Y_2O_3 ceramics [36].

Table 2. Thermal conductivities of 5.0 at% Yb:Y_2O_3 transparent ceramics prepared using different methods.

Sample	Synthesis of Powder	Consolidation	Sintering	Additives	Thermal Conductivity at RT ($W \cdot m^{-1} \cdot K^{-1}$)
5.0 at% Yb:Y_2O_3 [4]	solid-state reaction	dry pressing	vacuum sintering	3.0 at% ZrO_2 + 9.0 at% La_2O_3	6.50
5.0 at% Yb:Y_2O_3 [27]	solid-state reaction	dry pressing	vacuum sintering	3.0 at% ZrO_2	6.46
5.0 at% Yb:Y_2O_3 [16]	co-precipitation	dry pressing	vacuum sintering + HIP	1.0 at% ZrO_2	8.84
5.0 at% Yb:Y_2O_3 (This work)	solid-state reaction	centrifugal casting	air pre-sintering + HIP	none	9.94

The 5.0 at% Yb^{3+}-doped Y_2O_3 ceramic possessing the best optical transmittance was tested as a laser medium in the laser experiment. Figure 10 shows the measured output power versus the pump power of the laser. The laser had a threshold of about 41.2 mW. A slope efficiency of 4.3% was obtained from the linear fitting analysis. Benefiting from the pre-sintering in air and without any sintering additives, the sintered body was colorless. However, Li and Wang's study demonstrated that the absence of annealing treatment may

degrade lasing efficiency, attributable to excessive Yb^{2+} ions or oxygen vacancies in the crystal lattice [10]. Efforts are currently underway to examine whether the defects are the main factor that influences the laser performance and what the ramifications are for the mechanism of the Yb^{3+}-doped Y_2O_3 ceramic. Detailed results will be reported in our subsequent paper.

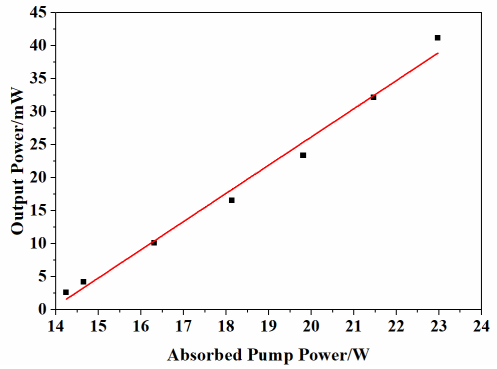

Figure 10. The output power vs. absorbed pump power for different output couplings of 5.0 at% Yb doped Y_2O_3 ceramic.

3. Materials and Methods

3.1. Powder Preparation

Commercial powders of Y_2O_3 (99.99% pure; Huizhou Ruier Rare Chemical Hi-Tech Co., Ltd., Huizhou, China) and Yb_2O_3 (99.99% pure; Huizhou Ruier Rare Chemical Hi-Tech Co., Ltd., Huizhou, China) were used as the starting material. The powders were weighted by the chemical composition of $(Yb_xY_{1-x})_2O_3$ (x = 0.01, 0.03, 0.05, 0.07) and then mixed in absolute ethyl alcohol for 12 h with zirconia balls. The mass ratio of balls to powder was 5:1. After drying at 110 °C for 6 h, the mixed powder was sieved through a 200-mesh nylon sieve. Then, the powder was calcined at 1100 °C for 4 h.

3.2. Suspension Preparation

A series of suspensions with different solid loadings were prepared by ball-milling Yb^{3+}-doped Y_2O_3 powder into deionized water and the deionization process, which has been proposed in [35]. After ball-milling the prepared Y_2O_3 suspension for 2 h, it was added to the apparatus made by our lab. Under the traction of a drainage pump, the suspension flowed through a chamber filled with deionized resin, where ions produced by Y_2O_3 hydrolysis were thoroughly absorbed by the resin. The treated suspension was then mixed with the addition of dispersant triammonium citrate (TAC, Sinopharm Chemical Reagent Co., Ltd., Beijing, China) of 1.25 wt% by mass of the Yb^{3+}-doped Y_2O_3 powder after the deionization process during ball milling.

3.3. Consolidation and Sintering

The consolidation of green compacts from the suspension was conducted by centrifugal slip casting. The suspension was centrifuged at 3000 rpm for 40 min. Then, it was dried at room temperature for 24 h and further dried at 110 °C for 12 h in an oven. Green compacts consolidated from the suspension after deionization were air pre-sintered at 1400 °C for 16 h in air and post-HIP at 1550 °C for 2 h under 200 MPa in an argon atmosphere. Samples of 5.0 at% Yb^{3+}-doped Y_2O_3 green compacts for the untreated suspension and deionized suspension were also prepared and then sintered under air condition at 1500 °C for 4 h to analyze the sintering mechanism.

3.4. Characterization

XRD (*X'*pert PROMPD, PANalytical, Almelo, The Netherlands) operating at 40 kV/50 mA using nickel-filtered CuKα radiation over a 2θ range of 15–60° with a scanning rate of 5°/min was adopted to identify the phase of the calcined powder. Transmission electron microscopy (TEM, Model JEM-2100 F, JEOL, Tokyo, Japan) was adopted to observe the morphologies of the calcinated powder. The particle size distribution of the suspension was measured by using a laser diffraction particle size analyzer (LA 920, Horiba, Irvine, CA, USA). The zeta potential of the suspension was characterized using an acoustic and electroacoustic spectrometer (DT-1202, Dispersion Technology Inc., Bedford Hills, NY, USA). The viscosity was measured by a cone-plate viscometer (Brookfield DV-II + Pro, Brookfield Engineering Laboratories, Middleboro, MA, USA). The concentration of Y species of the 5.0 at% Yb^{3+}-doped Y_2O_3 suspension of 10.0 wt% solid loading before and after deionization was tested by inductively coupled plasma optical emission spectroscopy (ICP) using an Optima 8300 ICP-OES system (PerkinElmer, Norwalk, VT, USA). Sample purification involved centrifugation at 3000 rpm for 10 min, and dual-stage filtration through 0.22 μm pore-size membranes, with the filtration process repeated for complete particle removal. Density measurements were performed via Archimedes' principle, with the relative density expressed as a percentage of theoretical density (5.03 g/cm^3). The morphology of the sintered bodies was observed by using a Hitachi scanning electron microscope (S4800, Hitachi, Tokyo, Japan). Nano measure software (version: 1.2) was adopted to measure the grain size of the samples, with at least 100 grains countered. Pellets with a thickness of 2.0 mm were sectioned from sintered samples and mirror-polished on both surfaces for optical characterization. In-line transmittance measurements were performed using a Perkin Elmer Lambda 750 S UV-Vis-NIR spectrophotometer (Model Lambda 750 S, Perkin Elmer, Shelton, CT, USA, for 200–2000 nm range) and a Thermo Scientific Nicolet iS5 FT-IR spectrometer (FT-IR, Nicolet iS5, Thermo Scientific, Madison, WI, USA, for 2.0–10.0 μm range). Thermal conductivity was determined for the 5.0 at% Yb:Y_2O_3 ceramic sample using a laser flash apparatus (LFA427 Nanoflash, Netzsch, Selb, Bavaria, Germany) at room temperature. The Vickers hardness, Hv, was measured using a hardness tester (450SVD™, Wilsonwolpert, Fort Worth, TX, USA) with an indentation load of 9.8 N. The fracture toughness (K_{IC}) of the ceramics was determined by the following equation:

$$K_{IC} = 0.016\left(\frac{l}{a}\right)^{-\frac{1}{2}}\left(\frac{E}{H}\right)^{\frac{2}{3}}P \quad (4)$$

where l is the crack length; $2a$ is the diagonal length of the indentation; $c = l + a$; H is the hardness value of the tested ceramics; P is the applied load; and E is the elastic modulus of the ceramics.

A 976 nm fiber-coupled diode laser (maximum power of about 26 W) served as the pump source. The 5.0 at% Yb^{3+}-doped Y_2O_3 ceramic was cut into a size of 10.0 mm in length and 3.0 mm × 3.0 mm in cross-sectional dimension. The input mirror was dichroic-coated with high reflectivity (R > 99.7%) at 1000–1100 nm and with high transmission for the pump wavelength. The output couplers exhibited 2.4% in transmission at 1000–1100 nm. The pump beam was focused onto the sample using a plano-convex lens. The sample, wrapped in indium foil for optimal thermal contact, was mounted in a water-cooled copper holder maintained at 18 °C via a recirculating chiller.

4. Conclusions

Aqueous colloidal processing through an easy deionization treatment to alleviate the hydrolysis issue was successfully introduced into the fabrication process of the Yb^{3+}-

doped Y_2O_3 ceramic. A well-dispersed suspension (35.0 vol%) with low viscosity was prepared, and it was found to be an excellent forming technology for preparing homogeneous green compacts with high relative density >50% as a consequence of high sintering activity. Furthermore, air pre-sintering at 1400 °C for 16 h yielded a pre-sintered body characterized by fine grain size and nano-scale closed pores uniformly distributed along grain boundaries, which significantly facilitated the subsequent HIP process. The samples doped with different concentrations (1.0, 3.0, 5.0, 7.0 at%) of Yb^{3+} with sub-micrometer levels (701–760 nm) and excellent optical and mechanical properties (Vickers hardness of 8.1–8.2 GPa) were achieved via low-temperature air pre-sintering plus HIP treatment without any sintering additive and annealing. The 5.0 at% Yb^{3+}-doped Y_2O_3 had an average grain size of 752 ± 25 nm and the transmittance reached 80.1% at 1100 nm and 83.0% in the mid-infrared region. The thermal conductivity was 9.94 $W \cdot m^{-1} \cdot K^{-1}$ and the laser output at 1076 nm reached a maximum power of 42 mW and a slope efficiency of 4.3%. Consequently, aqueous colloidal processing combined with deionization treatment offers a promising pathway to expand the forming technology of rare-earth-doped Y_2O_3 ceramics, particularly for high-power laser systems requiring low thermal impedance.

Author Contributions: Writing—original draft preparation, data curation, formal analysis, investigation, Q.W. and Z.F.; data curation, H.L.; supervision, N.W., J.L., Y.R. and Z.H. All authors have read and agreed to the published version of the manuscript.

Funding: This research was funded by the National Natural Science Foundation of China (No. 52302146), National Key Research and Development Program of China (No. 2021YFB3501700), and Scientific Study Project for Institutes of Higher Learning, Ministry of Education, Liaoning Province (No. LJ212411035022).

Institutional Review Board Statement: Not applicable.

Informed Consent Statement: Not applicable.

Data Availability Statement: The original contributions presented in this study are included in the article. Further inquiries can be directed to the corresponding author.

Acknowledgments: The authors thank Ma Jie and Wang Jun from the School of Jiangsu Normal University for the employment of their characterization equipment for the laser test.

Conflicts of Interest: Author Yi Ren was employed by the company Fujian Changting Golden Dragon Rare-Earth Co., Ltd. The remaining authors declare that the research was conducted in the absence of any commercial or financial relationships that could be construed as a potential conflict of interest.

References

1. Liu, Z.Y.; Ikesue, A.; Li, J. Research progress and prospects of rare-earth doped sesquioxide laser ceramics. *J. Eur. Ceram. Soc.* **2021**, *41*, 3895–3910. [CrossRef]
2. Yang, C.L.; Huang, J.Q.; Huang, Q.F.; Deng, Z.H.; Wang, Y.; Li, X.Y.; Zhou, Z.H.; Chen, J.; Liu, Z.G.; Guo, W. Optical, thermal, and mechanical properties of $(Y_{1-x}Sc_x)_2O_3$ transparent ceramics. *J. Adv. Ceram.* **2022**, *11*, 901–911. [CrossRef]
3. Brecher, C.; Wei, G.C.; Rhodes, W.H. Point defects in optical ceramics: High temperature absorption processes in lanthana-strengthened yttria. *J. Am. Ceram. Soc.* **1990**, *73*, 1473–1488. [CrossRef]
4. Zhang, L.; Pan, W.; Feng, J. Dependence of spectroscopic and thermal properties on concentration and temperature for Yb:Y_2O_3 transparent ceramics. *J. Eur. Ceram. Soc.* **2015**, *35*, 2547–2554. [CrossRef]
5. Takaichi, K.; Yagi, H.; Shirakawa, A.; Ueda, K.; Hosokawa, S.; Yanagitani, T.; Kaminskii, A.A. Lu_2O_3:Yb^{3+} ceramics—a novel gain material for high-power solid-state lasers. *Phys. Status Solidi* **2005**, *202*, R1–R3. [CrossRef]
6. Wang, X.L.; Shi, Y.L.; Lu, Z.H.; Zhang, C.; Chen, R.C.; Qi, J.Q.; Lu, T.C. Distinguishing the effects of lattice Gd^{3+} and segregated Gd^{3+} on optical properties of Yb:GdYAG transparent ceramics. *J. Eur. Ceram. Soc.* **2024**, *44*, 116722. [CrossRef]
7. Pirri, A.; Toci, G.; Patrizi, B.; Vannini, M. An overview on Yb-doped transparent polycrystalline sesquioxide laser ceramics. *IEEE J. Sel. Top. Quant. Electron.* **2018**, *24*, 1602108. [CrossRef]

8. Hou, X.R.; Zhou, S.M.; Li, Y.K.; Li, W.J. Effect of ZrO_2 on the sinterability and spectral properties of $(Yb_{0.05}Y_{0.95})_2O_3$ transparent ceramic. *Opt. Mater.* **2010**, *32*, 920–923. [CrossRef]
9. Kong, J.; Tang, D.Y.; Lu, J.; Ueda, K.; Yagi, H.; Yanagitani, T. Diode-end-pumped 4.2- W continuous-wave Yb:Y_2O_3 ceramic laser. *Opt. Lett.* **2004**, *29*, 1212–1214. [CrossRef]
10. Shirakawa, A.; Takaichi, K.; Yagi, H.; Bisson, J.-F.; Lu, J.; Musha, M.; Ueda, K.; Yanagitani, T.; Petrov, T.S.; Kaminski, A.A. Diode-pumped mode-locked Yb^{3+}:Y_2O_3 ceramic laser. *Optic Express* **2003**, *11*, 2911–2916. [CrossRef]
11. David, S.P.; Jambunathan, V.; Yue, F.; Lucianetti, A.; Mocek, T. Efficient diode pumped Yb:Y_2O_3 cryogenic laser. *Appl. Phys. B* **2019**, *125*, 137. [CrossRef]
12. Vorona, I.O.; Yavetskiy, R.P.; Doroshenko, A.G.; Parkhomenko, S.V.; Baumer, V.N.; Tolmachev, A.V.; Kosyanov, D.Y.; Vovna, V.I.; Kuryavyi, V.G.; Greculeasa, M.; et al. Structural-phase state and lasing of 5-15 at% Yb^{3+}:$Y_3Al_5O_{12}$ optical ceramics. *J. Eur. Ceram. Soc.* **2017**, *37*, 4115–4122. [CrossRef]
13. Zhang, X.; Huang, X.Y.; Liu, Z.Y.; Feng, Y.G.; Jiang, N.; Wu, L.X.; Yang, Z.X.; Xie, T.F.; Li, J. Fabrication, microstructure and properties of transparent Yb:Y_2O_3 ceramics from co-precipitated nanopowders. *Opt. Mater.* **2021**, *122*, 111792. [CrossRef]
14. Li, Q.; Wang, J.; Ma, J.; Ni, M.; Yang, F.; Liu, P.; Lee, K.Y.; Hsiang, H.-I.; Shen, D.Y.; Tang, D.Y. Fabrication of high-efficiency Yb:Y_2O_3 laser ceramics without photodarkening. *J. Am. Ceram. Soc.* **2022**, *105*, 3375–3381. [CrossRef]
15. Balabanov, S.; Permin, D.; Evstropov, T.; Andreev, P.; Basyrova, L.; Camy, P.; Baranov, M.; Mateos, X.; Loiko, P. Hot pressing of Yb:Y_2O_3 laser ceramics with LiF sintering aid. *Opt. Mater.* **2021**, *119*, 111349. [CrossRef]
16. Wang, J.; Ma, J.; Zhang, J.; Liu, P.; Luo, D.W.; Yin, D.L.; Tang, D.Y.; Kong, L.B. Yb:Y_2O_3 transparent ceramics processed with hot isostatic pressing. *Opt. Mater.* **2017**, *71*, 117–120. [CrossRef]
17. Lange, F.F. Powder processing science and technology for increased reliability. *J. Am. Ceram. Soc.* **1989**, *72*, 3–15. [CrossRef]
18. Olhero, S.M.; Ganesh, I.; Torres, P.M.C.; Alves, F.J.; Ferreira, J.M.F. Aqueous colloidal processing of ZTA composites. *J. Am. Ceram. Soc.* **2009**, *92*, 9–16. [CrossRef]
19. Lewis, J.A. Colloidal processing of ceramics. *J. Am. Ceram. Soc.* **2000**, *83*, 2341–2359. [CrossRef]
20. Yasrebi, M.; Zimek-Moroz, M.; Kemp, W.; Sturgis, D.H. Role of particle dissolution in stability of binary yttria-silica colloidal suspensions. *J. Am. Ceram. Soc.* **1996**, *79*, 1223–1227. [CrossRef]
21. Kuroda, Y.; Hamano, H.; Mori, T.; Yoshikawa, Y.; Nagao, M. Specific adsorption behavior of water on a Y_2O_3 surface. *Langmuir* **2000**, *16*, 6937–6947. [CrossRef]
22. Jin, L.L.; Mao, X.J.; Wang, S.W.; Dong, M.J. Optimization of the rheological properties of yttria suspensions. *Ceram. Int.* **2009**, *35*, 925–927. [CrossRef]
23. Sun, Z.Q.; Zhu, X.W.; Li, M.S.; Zhou, Y.C.; Sakka, Y. Hydrolysis and dispersion properties of aqueous $Y_2Si_2O_7$ suspensions. *J. Am. Ceram. Soc.* **2009**, *92*, 54–61. [CrossRef]
24. Ning, K.J.; Wang, J.; Luo, D.W.; Dong, Z.L.; Kong, L.B.; Tan, D.Y. Low-level sintering aids for highly transparent Yb:Y_2O_3 ceramics. *J. Alloys. Compd.* **2017**, *695*, 1414–1419. [CrossRef]
25. Yavetskiy, R.P.; Balabanov, A.E.; Parkhomenko, S.V.; Kryzhanovska, O.S.; Doroshenko, A.G.; Mateychenko, P.V.; Tolmachev, A.V.; Li, J.; Jiang, N.; Gheorghe, L.; et al. Effect of starting materials and sintering temperature on microstructure and optical properties of Y_2O_3:Yb^{3+} 5 at% transparent ceramics. *J. Adv. Ceram.* **2020**, *9*, 49–61. [CrossRef]
26. Ning, K.J.; Wang, J.; Ma, J.; Dong, Z.L.; Kong, L.B.; Tang, D.Y. Fabrication of laser grade Yb: Y_2O_3 transparent ceramics with ZrO_2 additive through hot isostatic pressing. *Mater. Today Commun.* **2020**, *24*, 101185. [CrossRef]
27. Hou, X.R.; Zhou, S.M.; Jia, T.T.; Lin, H.; Teng, H. Structural, thermal and mechanical properties of transparent Yb:$(Y_{0.97}Zr_{0.03})_2O_3$ ceramic. *J. Eur. Ceram. Soc.* **2011**, *31*, 733–738. [CrossRef]
28. Hou, X.R.; Zhou, S.M.; Li, W.J.; Li, Y.K. Study on the effect and mechanism of zirconia on the sinterability of yttria transparent ceramic. *J. Eur. Ceram. Soc.* **2010**, *30*, 3125–3129. [CrossRef]
29. Yoshida, H.; Kodo, M.; Soga, K.; Yamamoto, T. Doping effect on sinterability of polycrystalline yttria: From the viewpoint of cation diffusivity. *J. Eur. Ceram. Soc.* **2012**, *32*, 3103–3114. [CrossRef]
30. Bernard-Granger, G.; Guizard, C. Sintering behavior and optical properties of yttria. *J. Am. Ceram. Soc.* **2007**, *90*, 2698–2702. [CrossRef]
31. Xu, X.D.; Zhao, Z.W.; Xu, J.; Deng, P.Z. Thermal diffusivity, conductivity and expansion of $Yb_{3x}Y_{3(1-x)}Al_5O_{12}$ (x = 0.05, 0.1 and 0.25) single crystals. *Solid. State Commun.* **2004**, *130*, 529–532. [CrossRef]
32. Wang, J.; Yin, D.L.; Ma, J.; Liu, P.; Wang, Y.; Dong, Z.L.; Kong, L.B.; Tang, D.Y. Pump laser induced photodarkening in ZrO_2-doped Yb:Y_2O_3 laser ceramics. *J. Eur. Ceram. Soc.* **2019**, *39*, 635–640. [CrossRef]
33. Stanciua, G.; Gheorghea, L.; Voicua, F.; Haua, S.; Gheorghea, C.; Croitorua, G.; Enculescub, M.; Yavetskiy, R.P. Highly transparent Yb:Y_2O_3 ceramics obtained by solid-state reaction and combined sintering procedures. *Ceram. Int.* **2019**, *45*, 3217–3222. [CrossRef]
34. Liu, L.K.; Zhu, Q.H.; Zhu, Q.Q.; Jiang, B.X.; Feng, M.H.; Zhang, L. Fabrication of fine-grained undoped Y_2O_3 transparent ceramic using nitrate pyrogenation synthesized nanopowders. *Ceram. Int.* **2019**, *45*, 5339–5345. [CrossRef]

35. Fu, Z.C.; Li, X.D.; Zhang, M.; Zhu, Q.; Li, J.G.; He, J.; Wang, X.A.; Sun, X.D. Achieving fabrication of highly transparent Y_2O_3 ceramics via air pre-sintering by deionization treatment of suspension. *J. Am. Ceram. Soc.* **2021**, *104*, 2689–2701. [CrossRef]
36. Maruyama, M.; Okada, H.; Ochi, Y.; Nagashima, K. Sub-picosecond regenerative amplifier of Yb-doped Y_2O_3 ceramic thin disk. *Opt. Express* **2016**, *24*, 1685–1692. [CrossRef]
37. Yu, J.L.; Yang, J.L.; Huang, Y. The transformation mechanism from suspension to green body and the development of colloidal forming. *Ceram. Int.* **2011**, *37*, 1435–1451. [CrossRef]
38. Muller, R.H.; Mader, K.; Gohla, S. Solid lipid nanoparticles (SLN) for controlled drug delivery—A review of the state of the art. *Eur. J. Pharm. Biopharm.* **2000**, *50*, 161–177. [CrossRef]
39. Gouy, M. Sur la constitution de la charge électrique à la surface d'un electrolyte. *J. Phys. Theor. Appl.* **1910**, *9*, 457–468. [CrossRef]
40. Chapman, D.L. A contribution to the theory of electrocapillarity. *Lond. Edinb. Dublin Philos. Mag. J. Sci.* **1913**, *25*, 475–481. [CrossRef]
41. Saboorian-Jooybari, H.; Chen, Z. Calculation of re-defined electrical double layer thickness in symmetrical electrolyte solutions. *Results. Phys.* **2019**, *15*, 102501. [CrossRef]
42. Mondal, M.; Rai, V.K.; Srivastava, C.; Sarkar, S.; Akash, R. Enhanced frequency upconversion in $Ho^{3+}/Yb^{3+}/Li^{+}$:$YMoO_4$ nanophosphors for photonic and security ink applications. *J. Appl. Phys.* **2016**, *120*, 233101.1-11. [CrossRef]
43. Sanghera, J.; Kim, W.; Villalobos, G.; Shaw, B.; Baker, C.; Frantz, J.; Sadowski, B.; Aggarwal, I. Ceramic laser materials. *Materials* **2012**, *5*, 258–277. [CrossRef] [PubMed]

Disclaimer/Publisher's Note: The statements, opinions and data contained in all publications are solely those of the individual author(s) and contributor(s) and not of MDPI and/or the editor(s). MDPI and/or the editor(s) disclaim responsibility for any injury to people or property resulting from any ideas, methods, instructions or products referred to in the content.